

Validating a novel angular power spectrum estimator using simulated low frequency radio-interferometric data ¹

Samir Choudhuri

*Department of Physics, & Centre for Theoretical Studies, IIT Kharagpur, Pin: 721302, India
National Centre For Radio Astrophysics, Post Bag 3, Ganeshkhind, Pune 411007, India*

Nirupam Roy

Department of Physics, Indian Institute of Science, Bangalore 560012, India

Somnath Bharadwaj

Department of Physics and Meteorology & Centre for Theoretical Studies, IIT Kharagpur, 721302 India

Sk. Saiyad Ali

Department of Physics, Jadavpur University, Kolkata 700032, India

Abhik Ghosh

*Dept of Physics and Astronomy, University of the Western Cape, Robert Sobukwe Road, Bellville 7535, South Africa
SKA SA, The Park, Park Road, Pinelands 7405, South Africa*

Prasun Dutta

Department of Physics, IIT (BHU), Varanasi 221005, India

Abstract

The “Tapered Gridded Estimator” (TGE) is a novel way to directly estimate the angular power spectrum from radio-interferometric visibility data that reduces the computation by efficiently gridding the data, consistently removes the noise bias, and suppresses the foreground contamination to a large extent by tapering the primary beam response through an appropriate convolution in the visibility domain. Here we demonstrate the effectiveness of TGE in recovering the diffuse emission power spectrum through numerical simulations. We present details of the simulation used to generate low frequency visibility data for sky model with extragalactic compact radio sources and diffuse Galactic synchrotron emission. We then use different imaging strategies to identify the most effective option of point source subtraction and to study the underlying diffuse emission. Finally, we apply TGE to the residual data to measure the angular power spectrum, and assess the impact of incomplete point source subtraction in recovering the input power spectrum C_ℓ of the synchrotron emission. This estimator is found to successfully recovers the C_ℓ of input model from the residual visibility data. These results are relevant for measuring the diffuse emission like the Galactic synchrotron emission. It is also an important step towards characterizing and removing both diffuse and compact foreground emission in order to detect the redshifted 21 cm signal from the Epoch of Reionization.

¹©2017. This manuscript version is made available under the CC-BY-NC-ND 4.0 license <http://creativecommons.org/licenses/by-nc-nd/4.0/>

Keywords: methods: statistical; methods: data analysis; techniques: interferometric; (cosmology:) diffuse radiation

1. Introduction

A detailed investigation and analysis of the Galactic diffuse synchrotron emission power spectrum can be used to study the distribution of cosmic ray electrons and the magnetic fields in the interstellar medium (ISM) of the Milky Way, and is very interesting in its own right (Waelkens et al., 2009; Lazarian & Pogosyan, 2012; Iacobelli et al., 2013). On the other hand, at a very different scale, observations of redshifted 21 cm radiation from neutral hydrogen (HI) hold the potential of tracing the large scale structure of the Universe over a large redshift range of $200 \geq z \geq 0$. Accurate cosmological HI tomography and power spectrum measurement, particularly from the Epoch of Reionization (EoR), by ongoing or future low-frequency experiments will provide us a significant amount of information about various astrophysical and cosmological phenomena to enhance our present understanding of the Universe. Interestingly, since one of the main challenges in statistical detection of the redshifted 21 cm signal arises from the contamination by Galactic and extragalactic “foregrounds” (Shaver et al., 1999; Di Matteo et al., 2002; Santos et al., 2005), these two aspects are also quite related. The two major foreground components for cosmological HI studies are (1) the bright compact (“point”) sources and (2) the diffuse Galactic synchrotron emission (Ali, Bharadwaj & Chengalur, 2008; Paciga et al., 2011; Bernardi et al., 2009; Ghosh et al., 2012; Iacobelli et al., 2013). Detection of the weak cosmological HI signal will require a proper characterization and removal of point sources as well as this diffuse foregrounds.

Naturally, a significant amount of effort has gone into addressing the problem of foreground removal for detecting the 21 cm power spectrum from EoR (Morales et al., 2006; Jelić et al., 2008; Liu et al., 2009a,b; Harker et al., 2010; Mao, 2012; Liu & Tegmark, 2012; Chapman et al., 2012; Paciga et al., 2013). In contrast, foreground avoidance (Datta et al., 2010a; Vedantham et al., 2012; Morales et al., 2012; Trott et al., 2012; Parsons et al., 2012; Pober et al., 2013; Dillon et al., 2013; Hazelton et al., 2013; Thyagarajan et al., 2013; Liu et al., 2014a,b; Ali et al., 2015; Trott et al., 2016) is an alternative approach based on the idea that contamination from any foreground with smooth spectral behaviour is confined only to a wedge in cylindrical $(k_{\perp}, k_{\parallel})$ space due to chromatic coupling of an interferometer with the foregrounds. The HI power spectrum can be estimated from the uncontaminated modes outside the wedge region termed as the *EoR window* where the HI signal is dominant over the foregrounds. With their merits and demerits, these two approaches are considered complementary (Chapman et al., 2016).

Here we have considered the issue of estimating the angular power spectrum directly from the radio-interferometric “visibility” data. In this endeavor, we have developed a novel and fast estimator of angular power spectrum that consistently avoids the noise bias, and tested it with simulated diffuse Galactic synchrotron emission (Choudhuri et al., 2014). Here, we have further developed the simulations to include the point sources in the sky model (as well as instrumental noise) to investigate the effectiveness of the estimator of recovering the diffuse emission power spectrum in presence of the point sources. This paper describes the details of the simulations and

Email address: samir11@phy.iitkgp.ernet.in (Samir Choudhuri)

analysis, including the adopted point source modeling and subtraction strategies, and their effects on the residual diffuse emission. We demonstrate that, by using this newly developed Tapered Gridded Estimator (hereafter TGE), we can avoid some of the complications of wide field low frequency imaging by suitably tapering the primary beam during power spectrum estimation. A companion paper has reported the usefulness of the new estimator in recovering the diffuse emission power spectrum from the residual data in such situation (Choudhuri et al., 2016a). A further generalization of the estimator to deal with spherical and cylindrical power spectrum is presented in Choudhuri et al. (2016b). Please note that this is part of a coherent effort of end-to-end simulation of realistic EoR signal and foreground components, and finally using suitable power spectrum estimator to recover the signal. However, even though these exercises are in the context of EoR experiments, for the sake of simplicity, we have so far not included the weak cosmological signal in the model. Here we establish the ability of the developed estimator to recover the diffuse emission power spectrum accurately after point source subtraction. Thus, apart from EoR experiments, these results are also relevant in more general situation, e.g. detailed study of Galactic synchrotron emission (Choudhuri et al., 2017).

The current paper is organized as follows. In Section 2, we discuss the details of the point source and diffuse emission simulation. Section 3 and 4 present the analysis using different CLEANing options for point source subtraction and the results of power spectrum estimation. Finally, we present summary and conclusions in section 5.

2. Multi-frequency Foreground Simulation

In this section we describe the details of the foreground simulation to produce the sky model for generating visibilities for low radio frequency observation with an interferometer. Even if the simulation, described in this paper, is carried out specifically for 150 MHz observation with the Giant Metrewave Radio Telescope (GMRT), it is generic and can easily be extended to other frequency and other similar telescopes including the Square Kilometre Array (SKA).

Earlier studies (Ali, Bharadwaj & Chengalur, 2008; Paciga et al., 2011) have found that, for 150 MHz GMRT small field observations, the bright compact sources are the dominating foreground component for EoR signal at the angular scales $\leq 4^\circ$, the other major component being the Galactic diffuse synchrotron emission (Bernardi et al., 2009; Ghosh et al., 2012; Iacobelli et al., 2013). We build our foreground sky model keeping close to the existing observational findings. The sky model includes the main two foreground components (i) discrete radio point sources and (ii) diffuse Galactic synchrotron emissions. The contributions from these two foregrounds dominate in low frequency radio observations and their strength is $\sim 4 - 5$ orders of magnitude larger than the $\sim 20 - 30$ mK cosmological 21-cm signal (Ali, Bharadwaj & Chengalur, 2008; Ghosh et al., 2012). Galactic and extragalactic free-free diffuse emissions are also not included in the model, though each of these is individually larger than the HI signal.

2.1. Radio Point Sources

Most of the earlier exercise of numerical simulation conducted so far have not included the bright point source foreground component in the multi-frequency model. In such analysis, it is generally assumed that the brightest point sources are perfectly subtracted from the data before the main analysis, and the simulated data contains only faint point sources and other diffuse foreground components, HI signal and noise. We, however, simulate the point source distribution

for sky model using the following differential source counts obtained from the GMRT 150 MHz observation (Ghosh et al., 2012):

$$\frac{dN}{dS} = \frac{10^{3.75}}{\text{Jy.Sr}} \left(\frac{S}{\text{Jy}} \right)^{-1.6}. \quad (1)$$

The full width half maxima (FWHM) of the GMRT primary beam (PB) at 150 MHz is $\approx 3.1^\circ$. To understand and quantify how the bright point sources outside the FWHM of the PB affect our results, we consider here a larger region ($7^\circ \times 7^\circ$) for point source simulation. Initially, 2215 simulated point sources, with flux density in the range 9 mJy to 1 Jy following the above mentioned source count, are randomly distributed over this larger region. Out of those sources, 353 are within $95'$ from the phase centre (where the PB response falls by a factor of e). We note that the antenna response falls sharply after this radius. For example, the primary beam response is $\lesssim 0.01$ in the first sidelobe. Hence, outside this “inner” region, only sources with flux density greater than 100 mJy are retained for the next step of the simulation. In the outer region, any source fainter than this will be below the threshold of point source subtraction due to primary beam attenuation. With 343 sources from the “outer” region, we finally include total 696 sources in our simulation. Figure 1 shows the angular positions of all 2215 sources over this region, as well as of the 696 sources after the flux density restriction. Note that, we have assumed all the sources are unresolved at the angular resolution of our simulation. In reality, there will also be extended sources in the field. Some of the extended sources can be modelled reasonably well as collection of multiple unresolved sources. However, other complex structures will need more careful modelling or masking, and are not included in this simulation for simplicity.

The flux density of point sources changes across the frequency band of observation. We scale the flux density of the sources at different frequencies using the following relation,

$$S_\nu = S_{\nu_0} \left(\frac{\nu}{\nu_0} \right)^{-\alpha_{\text{ps}}} \quad (2)$$

where $\nu_0 = 150$ MHz is the central frequency of the band, ν changes across the bandwidth of 16MHz and α_{ps} is the spectral index of point sources. The point sources are allocated a randomly selected spectral index uniform in the range of 0.7 to 0.8 (Jackson, 2005; Randall et al., 2012). Please note that the subsequent point source modeling and subtraction are carried out in such a way that the final outcomes do not depend on the exact distribution function of the spectral index.

2.2. Diffuse Synchrotron Emission

In this section, we first describe the simulation of the diffuse Galactic synchrotron emission which are used to generate the visibilities. The angular slope β of the angular power spectrum of diffuse Galactic synchrotron emission is within the range 1.5 to 3 as found by all the previous measurements at frequency range 0.15 – 94 GHz (e.g. Tegmark & Efstathiou 1996; Tegmark et al. 2000; Giardino et al. 2002; Bennett et al. 2003; La Porta et al. 2008; Bernardi et al. 2009; Ghosh et al. 2012; Iacobelli et al. 2013; Choudhuri et al. 2017). For the purpose of this paper, we assume that the fluctuations in the diffuse Galactic synchrotron radiation are coming from a statistically homogeneous and isotropic Gaussian random field whose statistical properties are completely specified by the angular power spectrum. We construct our sky model of the diffuse Galactic synchrotron emission using the measured angular power spectrum at 150 MHz (Ghosh et al., 2012)

$$C_\ell^M(\nu) = A_{150} \times \left(\frac{1000}{\ell} \right)^\beta \times \left(\frac{\nu}{150\text{MHz}} \right)^{-2\alpha_{\text{syn}}}, \quad (3)$$

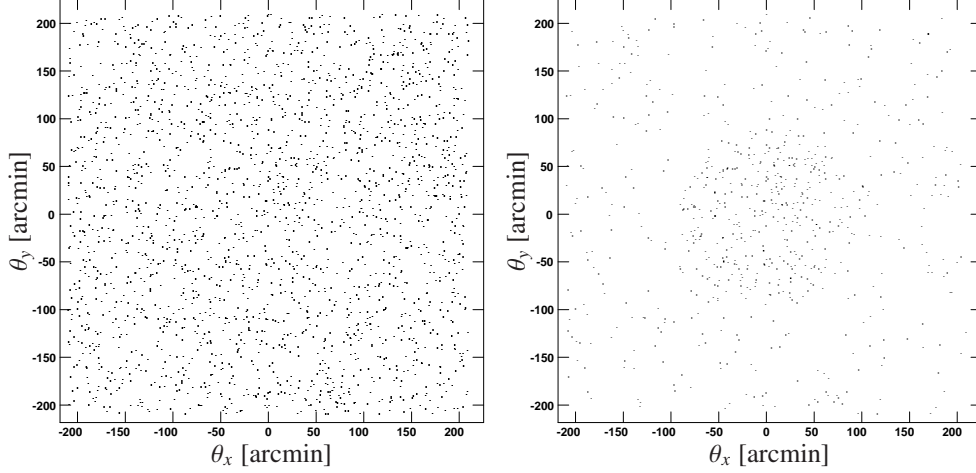


Figure 1: The angular position of the simulated point sources over a $7^\circ \times 7^\circ$ region. The left panel shows positions of all 2215 sources over this whole field, and the right panel shows 696 sources after applying a flux density cutoff. The number of point sources in the flux density range 9 mJy to 1 Jy inside the FWHM of the primary beam is $N_{in} = 353$ and outside of the FWHM with flux density more than 100 mJy is $N_{out} = 343$.

where ν is the frequency in MHz, $A_{150} = 513 \text{ mK}^2$ and $\beta = 2.34$ adopted from Ghosh et al. (2012) and $\alpha_{\text{syn}} = 2.8$ from Platania et al. (1998). The diffuse emissions are generated in a 1024×1024 grid with angular grid size of $\sim 0.5'$, covering a region of $8.7^\circ \times 8.7^\circ$. This axis dimension is ≈ 2.8 times larger than the FWHM of the GMRT primary beam.

To simulate the diffuse emission, we mainly followed the same procedure as discussed in Choudhuri et al. (2014). We first create the Fourier components of the temperature fluctuations on a grid using

$$\Delta\tilde{T}(\mathbf{U}, \nu_0) = \sqrt{\frac{\Omega C_\ell^M(\nu_0)}{2}} [x(\mathbf{U}) + iy(\mathbf{U})], \quad (4)$$

where Ω is the total solid angle of the simulated area, and $x(\mathbf{U})$ and $y(\mathbf{U})$ are independent Gaussian random variables with zero mean and unit variance. Then, we use the Fastest Fourier Transform in the West (hereafter FFTW) algorithm (Frigo et al., 2005) to convert $\Delta\tilde{T}(\mathbf{U}, \nu_0)$ to the brightness temperature fluctuations $\delta T(\vec{\theta}, \nu_0)$ or, equivalently, the intensity fluctuations $\delta I(\vec{\theta}, \nu_0)$ on the grid. The intensity fluctuations $\delta I(\vec{\theta}, \nu) = (2k_B/\lambda^2) \delta T(\vec{\theta}, \nu)$ can be calculated using the Rayleigh-Jeans approximation which is valid at the frequency of our interest.

Finally, we generate the specific intensity fluctuations at any other frequency within the observing band from that of the reference frequency using the scaling relation

$$\delta I(\vec{\theta}, \nu) = (2k_B/\lambda^2) \delta T(\vec{\theta}, \nu_0) \left(\frac{\nu}{\nu_0}\right)^{-\alpha_{\text{syn}}}. \quad (5)$$

In general, the spectral index α_{syn} of the diffuse emission may have a spatial variation and the synchrotron power spectrum may be different at different frequencies. However, the effect of this

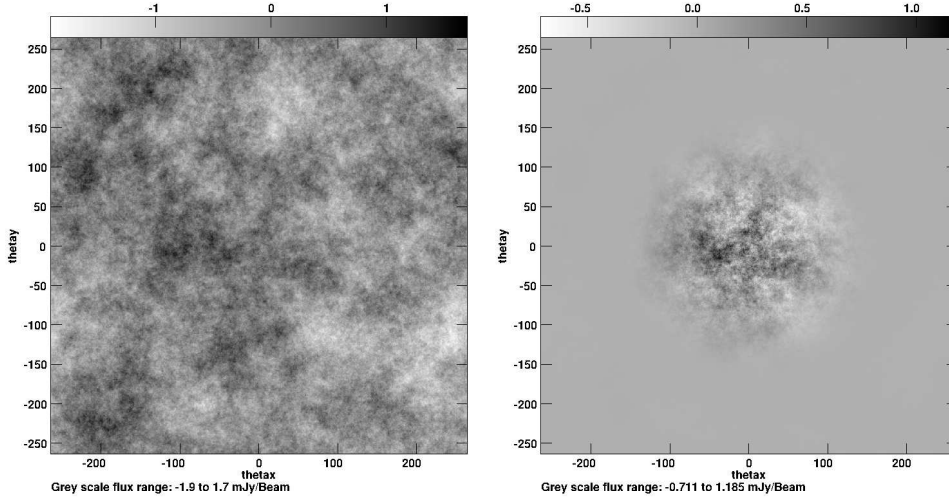


Figure 2: The simulated 150 MHz diffuse emission map before (left panel) and after (right panel) multiplying the GMRT primary beam. The images are $8.7^\circ \times 8.7^\circ$ with a grid size $\sim 0.5'$, and the grey scale is in mJy/Beam.

on point source subtraction is expected to be negligible, and the final results do not depend on the constancy of the synchrotron power spectrum slope. Here, we assume that the value of α_{syn} is fixed over the whole region and across the observation band in the multi-frequency simulation.

2.3. GMRT Primary beam

We model the PB of GMRT assuming that the telescope has an uniformly illuminated circular aperture of 45 m diameter (D) whereby the primary beam pattern is given by,

$$\mathcal{A}(\vec{\theta}, \nu) = \left[\left(\frac{2\lambda}{\pi\theta D} \right) J_1 \left(\frac{\pi\theta D}{\lambda} \right) \right]^2 \quad (6)$$

where J_1 is the Bessel function of the first kind of order one. The primary beam pattern is normalized to unity at the pointing center [$\mathcal{A}(0) = 1$]. The central part of the model PB (eq. 6) is a reasonably good approximation to the actual PB of the GMRT antenna, whereby, it may vary at the outer region. In our analysis, we taper the outer region through a window function, hence the results are not significantly affected by the use of this approximate model PB.

Figure 2 shows one realization of the intensity fluctuations $\delta I(\vec{\theta}, \nu_0)$ map at the central frequency $\nu_0 = 150$ MHz with and without multiplication of the GMRT primary beam. The PB only affect the estimated angular power spectrum at large angular scales ($\lesssim 45 \lambda$) which is shown in Figure 3 of Choudhuri et al. (2014). Using a large number of realizations of the diffuse emission map, we find that the recovered angular power spectrum is in good agreement with the input model power spectrum (eq. 3) at the scales of our interest ($\ell \sim 300 - 2 \times 10^4$).

2.4. Simulated GMRT Observation

The simulations are generated keeping realistic GMRT specifications in mind, though these parameters are quite general, and similar mock data for any other telescope can be generated

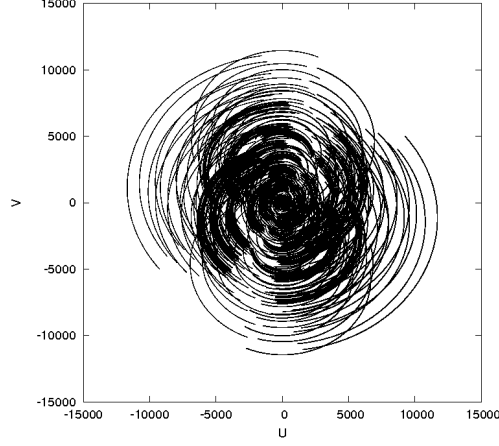


Figure 3: The GMRT uv coverage with phase centre at R.A.=10h46m00s Dec=59°00′59″ for a total observation time of 8hr. Note that u and v are projected antenna separations in units of wavelength at the central frequency 150 MHz.

easily. The GMRT has 30 antennas. The diameter of each antenna is 45m. The projected shortest baseline at the GMRT can be 60m, and the longest baseline is 26 km. The instantaneous bandwidth is 16 MHz, divided into 128 channels, centered at 150 MHz. We consider all antennas pointed to an arbitrary field located at R.A.=10h46m00s Dec=59°00′59″ for a total of 8 hr observation. The visibility integration time was chosen as 16 s. The mock observation produces 783000 samples per channels in the whole uv range. Figure 3 shows the full uv coverage at central frequency for the simulated GMRT Observation.

The angular power spectrum of the diffuse synchrotron emission (eq. 3) declines with increasing baseline $U = |\mathbf{U}|$ (where $\ell = 2\pi U$), and drops significantly at the available longest baseline. Hence, for our simulation, the contributions of the diffuse emission have been taken from only baselines $U \leq 3,000 \lambda$ to reduce the computation time. To calculate the visibilities, we multiply the simulated intensity fluctuations $\delta I(\vec{\theta}, \nu)$ with the PB (eq. 6), and we use 2-D FFTW of the product in a grid. For each sampled baseline $U \leq 3,000 \lambda$, we interpolate the gridded visibilities to the nearest baseline of the uv track in Figure 3. We notice that the w -term does not have significant impact on the estimated angular power spectrum of diffuse synchrotron emission (Choudhuri et al., 2014). But, to make the image properly and also to reduce the sidelobes of the point spread function (or the synthesized beam), it is necessary to retain the w -term information. The w -term also improves the dynamic range of the image and enhances the precision of point source subtraction. We use the full baseline range to calculate the contribution from the point sources. The sky model for the point sources is multiplied with PB $\mathcal{A}(\vec{\theta}, \nu)$ before calculating the visibilities. Using the small field of view approximation, the visibilities for point sources are computed at each baseline by incorporating the w term:

$$V(\mathbf{U}, \nu) \approx \int d^2\theta \mathcal{A}(\vec{\theta}, \nu) \delta I(\vec{\theta}, \nu) e^{-2\pi i(u\theta_x + v\theta_y + w(\sqrt{1-\theta_x^2 - \theta_y^2} - 1))}. \quad (7)$$

The system noise of the interferometer is considered to be independent at different baselines and channels, and is modelled as Gaussian random variable. We add independent Gaussian

random noise to both the real and imaginary parts of each visibility. For a single polarization, the theoretical rms noise in the real or imaginary part of a measured visibility is

$$\sigma = \frac{\sqrt{2}k_B T_{sys}}{A_{eff} \sqrt{\Delta\nu\Delta t}} \quad (8)$$

where T_{sys} is the total system temperature, k_B is the Boltzmann constant, A_{eff} is the effective collecting area of each antenna, $\Delta\nu$ is the channel width and Δt is correlator integration time (Thompson, Moran & Swenson, 1986). For $\Delta\nu = 125$ kHz and $\Delta t = 16$ sec, the rms noise comes out to be $\sigma_n = 1.03$ Jy per single polarization visibility for GMRT. The two polarizations are assumed to have identical sky signals but independent noise contribution.

In summary, the simulated visibilities for the GMRT observation are sum of two independent components namely the sky signal and the system noise. As outlined above, the realistic sky signal includes the extragalactic point sources and the Galactic diffuse synchrotron emission. The visibility data does not contain any calibration errors, ionospheric effects and radio-frequency interference (RFI), and a detailed investigation of these effects are left for future work.

3. Data Analysis

Our next goal is to analyze the simulated data described above to recover the statistical properties of the diffuse emission, and compare those with the known input model parameters. As mentioned earlier, to estimate the power spectrum of the diffuse emission, our approach is to first remove the point source foreground accurately. This requires imaging and deconvolution to model the point sources, and then subtracting them from the data. In reality, there are many issues which make an accurate subtraction of point sources from radio interferometric wide-field synthesis images challenging. These include residual gain calibration errors (Datta et al., 2010), direction dependence of the calibration due to instrumental or ionospheric/atmospheric conditions (Intema et al., 2009; Yatawatta, 2012), the effect of spectral index of the sources (Rau & Cornwell, 2011), frequency dependence and asymmetry of the primary beam response, varying point spread function (synthesized beam) of the telescope (Liu et al., 2009a; Morales et al., 2012; Ghosh et al., 2012), high computational expenses of imaging a large field of view, and CLEANing a large number of point sources (particularly severe at low radio frequency images, Pindor et al., 2011) etc. Note that these issues are more prominent at low radio frequencies due to a comparatively large field of view as well as a large number of strong point sources and bright Galactic synchrotron emission. Hence, foreground is one of the major problem particularly in the context of EoR and post-EoR cosmological HI studies with the current and future telescopes (e.g. GMRT², LOFAR³, MWA⁴, PAPER⁵, PaST⁶, HERA⁷, and SKA⁸).

Earlier, Datta et al. (2009, 2010) have studied the effect of calibration errors in bright point source subtraction. They have concluded that, to detect the EoR signal, sources brighter than

²Giant Metrewave Radio Telescope; <http://www.gmrt.ncra.tifr.res.in>

³Low Frequency Array; <http://www.lofar.org>

⁴Murchison Wide-field Array; <http://www.mwatelescope.org>

⁵Precision Array to Probe the Epoch of Reionization; <http://astro.berkeley.edu/dbacker/eor>

⁶Primeval Structure Telescope; <http://web.phys.cmu.edu/past>

⁷Hydrogen Epoch of Reionization Array; <http://reionization.org/>

⁸Square Kilometer Array; <http://www.skatelescope.org>

1 Jy should be subtracted with a positional accuracy better than 0.1 arcsec if calibration errors remain correlated for a minimum time ~ 6 hours of observation. On the other hand, Bowman et al. (2009) and Liu et al. (2009b) have reported that point sources should be subtracted down to a 10–100 mJy threshold in order to detect the 21 cm signal from the EoR. It has also been recently demonstrated using both simulated and observed data from MWA that foreground (particularly the point sources) must be considered as a wide-field contaminant to measure the 21 cm power spectrum (Pober et al., 2016). The polarized galactic synchrotron emission is expected to be Faraday-rotated along the path, and it may acquire additional spectral structure through polarization leakage at the telescope. This is a potential complication for detecting the HI signal (Jelić et al., 2010; Moore et al., 2013). To cope with the capabilities of current and forthcoming radio telescopes, recently there have been a significant progress in developing calibration, imaging and deconvolution algorithms (Bhatnagar et al., 2013; Cornwell et al., 2008) which can now handle some of the above-mentioned complications.

Keeping aside calibration errors, the problem of subtracting point sources ultimately reduces to a problem of deconvolution of point sources, in presence of diffuse (foreground and/or cosmological HI signal) emission, to fit their position, flux density and spectral property as accurately as the instrumental noise permits. The optimum strategy of modeling and subtracting point sources in presence of diffuse emission is an open question in the general context of interferometric radio frequency data analysis. In this paper, we take up a systematic analysis of the 150 MHz simulated data to quantify effect of incomplete spectral modeling and of different deconvolution strategies to model and subtract point sources for recovering the diffuse emission power spectrum. In particular, we demonstrate the advantage of the power spectrum estimator that we have used (TGE) which allow us to avoid wide field imaging in order to subtract the point sources from the outer part of the field of view. As a result, it also takes care of, at least to a large extent, issues like asymmetry of the primary beam, direction dependence of the calibration for the outer region of the field of view and high computational expenses of imaging and removing point sources from a large field of view etc. Below we describe the details of the imaging and point source subtraction used to produce the residual visibility data for power spectrum estimation.

3.1. Imaging and Power spectrum Estimation

For our analysis, we use the Common Astronomy Software Applications (CASA)⁹ to produce the sky images from the simulated visibility data. To make a CLEAN intensity image, we use the Cotton-Schwab CLEANing algorithm (Schwab, 1984) with Briggs weighting and robust parameter 0.5, and with different CLEANing thresholds and CLEANing boxes around point sources. The CLEANing is also done with or without multifrequency synthesis (MFS; Sault & Wieringa 1994; Conway et al. 1990; Rau & Cornwell 2011). If MFS is used during deconvolution, it takes into account the spectral variation of the point sources using Taylor series coefficients as spectral basis functions. In a recent paper Offringa et al. (2016) suggest that CASA’s MS-MFS algorithm can be used for better spectral modelling of the point sources. The large field of view ($\theta_{FWHM} = 3.1^\circ$) of the GMRT at 150 MHz lead to significant amount of errors if the non-planar nature of the GMRT antenna distribution is not taken into account. For this purpose we use w -projection algorithm (Cornwell et al., 2008) implemented in CLEAN task within the CASA. For different CLEANing strategies, we assess the impact of point sources removal in recovering the input angular power spectrum C_ℓ of diffuse Galactic synchrotron emission from

⁹<http://casa.nrao.edu/>

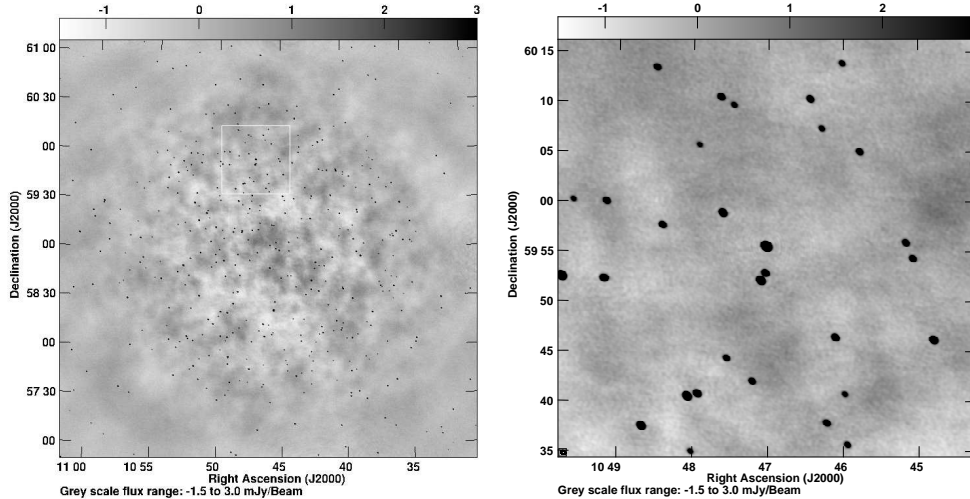


Figure 4: The left panel shows the CLEANed image ($4.2^\circ \times 4.2^\circ$) of the simulated sky centered at R.A.=10h46m00s Dec=59°00′59″. The synthesized beam has a FWHM $\sim 20''$. A zoom of the square region, $42' \times 42'$ in size, marked in the left panel is shown in the right panel. This representative region is used in Figure 6 for comparison of “residual” images. In the central region the “off-source” rms noise is ≈ 0.3 mJy/Beam. Here, the grey scale is in units of mJy/Beam.

residual uv data. Effectively, by CLEANing with these different options, we identify the optimum approach to produce the best model for point source subtraction and C_ℓ estimation. We investigate the CLEANing effects in the image domain by directly inspecting the “residual images” after the point source subtraction, and also in the Fourier domain by comparing the power spectrum of the residual data with the input power spectrum of the simulated diffuse emission. For discussion on some of the relevant methods and an outline of the power spectrum estimation, please see Choudhuri et al. (2014) and references therein.

The left panel of Figure 4 shows the CLEANed image of the simulated sky of the target field with angular size $4.2^\circ \times 4.2^\circ$. The synthesized beam has a FWHM $\sim 20''$. The image contains both point sources and diffuse synchrotron emission, and the grey scale flux density range in Figure 4 is saturated at 3 mJy to clearly show the diffuse emission. The inner part ($\approx 1.0^\circ \times 1.0^\circ$) of CLEANed image has rms noise ≈ 0.3 mJy/Beam, and it drops to ≈ 0.15 mJy/Beam at the outer part due to the response of the GMRT primary beam attenuation. In the right panel of Figure 4, we also show a small portion (marked as a square box in the left panel) of the image with an angular size $42' \times 42'$. We note that there is a strong point source at the centre of this small image with a flux density of 676 mJy/Beam and spectral index of 0.77. The intensity fluctuations of the diffuse emission are also clearly visible in both the panels of Figure 4.

Figure 5 shows the angular power spectrum C_ℓ estimated from the simulated visibilities before any point source subtraction. We find that the estimated power spectrum, as expected, is almost flat across all angular scales. This is the Poisson contribution from the randomly distributed point sources which dominate C_ℓ at all angular multipoles ℓ in our simulation. In this paper, we do not include the clustering component of the point sources which becomes dominant only at large angular scales ($\ell \leq 900$) (Ali, Bharadwaj & Chengalur, 2008) where it introduces

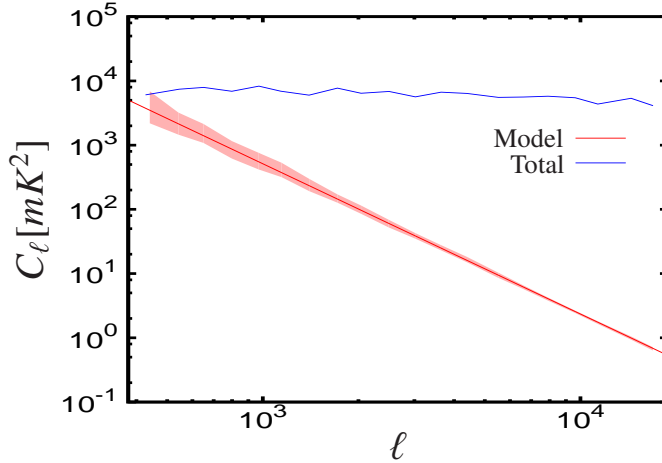


Figure 5: The angular power spectrum C_ℓ estimated from the visibility data which contains both point sources and diffuse synchrotron emission. This spectrum, dominated by the point sources, is flat due to the Poisson distribution of positions of the point sources in our simulation. For comparison, we show the model synchrotron power spectrum (lower curve) with $1\text{-}\sigma$ error estimated from 100 realizations of the diffuse emission map.

a power law ℓ dependence in the angular power spectrum. We also note that the convolution with the primary beam affects the estimated angular power spectrum at small ℓ values (Figure 3, Choudhuri et al. 2014), and it will be difficult to individually distinguish the Poisson and the clustered part of the point source components with the GMRT. The total simulated power spectrum C_ℓ (Figure 5) is consistent with the previous GMRT 150 MHz observations (Ali, Bharadwaj & Chengalur 2008; Ghosh et al. 2012). In Figure 5 we also show the input model angular power spectrum of the diffuse emission along with $1\text{-}\sigma$ error bar (shaded region) estimated from 100 realizations of the diffuse emission map. Note that the angular power spectrum of the diffuse emission is buried deep under the point source contribution which dominates at all angular scales accessible to the GMRT. We emphasize that, in this paper, our aim is to recover this diffuse power spectrum from the residual visibility data after point source subtraction.

3.2. Point Source Subtraction

As shown in Figure 5, the 150 MHz radio sky is dominated by point sources at the angular scales $\leq 4^\circ$ (Ali, Bharadwaj & Chengalur, 2008). Therefore, it is very crucial to identify all point sources precisely from the image, and remove their contribution from the visibility data in order to estimate the power spectrum of background diffuse emission. However, it is quite difficult to model and subtract out the point sources from the sidelobes and the outer parts of the main lobe of the primary beam. Our recent paper (Choudhuri et al., 2016a) contains a detailed discussion of the real life problems for modelling and subtracting point sources from these regions. In this paper we have restricted the point source subtraction to the central region of the primary beam. To estimate the angular power spectrum C_ℓ from the visibilities, we have used the TGE which tapers the sky response to suppress the effect of the point sources outside the FWHM of the primary beam. This is achieved by convolving the visibilities with a window function. Note that the TGE is also an *unbiased* estimator for the angular power spectrum C_ℓ ; it calculates and subtracts the noise bias self-consistently (see Choudhuri et al., 2014, for details). Below we discuss the

Name	<i>nterms</i>	Threshold flux density	CLEANing Box
Run(a)	1	1.0 mJy	Single $4.2^\circ \times 4.2^\circ$ Box
Run(b)	2	1.0 mJy	Single $4.2^\circ \times 4.2^\circ$ Box
Run(c)	2	0.5 mJy	Single $4.2^\circ \times 4.2^\circ$ Box
Run(d)	2	2.0 mJy	Single $4.2^\circ \times 4.2^\circ$ Box
Run(e)	2	0.5 mJy	Circular region with radius $50''$ around all sources in the image
Run(f)	2	2.0 mJy 0.5 mJy	Single $4.2^\circ \times 4.2^\circ$ Box $1.6' \times 1.6'$ Box around each visible residual sources

Table 1: The set of parameters used for point source imaging with different CLEANing strategies.

point source modeling and the effect of different CLEANing strategies on the “residual” images created from the point source subtracted visibility data.

We use standard CASA task CLEAN and UVSUB for deconvolution and removal of point sources from the visibility data respectively. CLEAN identifies pixels with flux density over the specified threshold, do the deconvolution and create the corresponding model visibilities, while UVSUB produce the residual visibility by subtracting the model. This should remove the point source contribution from the data to a large extent. We further use the residual visibility after point source subtraction to make residual “dirty” images (without deconvolution) of size $4.2^\circ \times 4.2^\circ$. This is done using various CLEANing threshold (0.5, 1.0 and 2.0 mJy where $1 \text{ mJy} \approx 3\sigma_{im}$), CLEAN box, and spectral modelling options for comparison. For CLEAN box, we tried CLEANing the *whole* image up to the threshold, or use circular boxes of radius $50''$ around *all* point sources. As expected, the former is more computation expensive and also removes some positive and negative peaks of the diffuse signal. On the other hand, the later requires a pre-existing deep point source catalogue with accurate position of the sources. Note that while such low frequency catalogues for EoR experiments may be available from deep continuum surveys in near future, at present it is not a realistic strategy. We also used a hybrid method by first CLEANing the whole image up to a conservative flux density threshold, and then placing rectangular CLEAN boxes of size $1.6' \times 1.6'$ around all residual point sources identified visually. These selected regions are then CLEANed up to a deeper flux density limit. The effect of spectral modelling is checked by changing the parameter “*nterms*” in the CASA task CLEAN where *nterms*=1 does not include any spectral correction, while *nterms*=2 builds the point source model by including spectral index during multi-frequency CLEANing (Rau & Cornwell, 2011).

Table 1 lists the parameters for a set of CLEANing and point source subtraction runs we used for comparison. Figure 6 shows a representative region of angular size $42' \times 42'$ from the dirty images of the residual data, to illustrate the effect of different cleaning schemes. The different residual images (Image(a) to Image(f)) in Figure 6 correspond to the different CLEANing strategies in Table 1 (Run(a) to Run(f)). The residual images are mostly dominated by the diffuse emissions. As expected, correct spectral modelling of the point sources significantly improves the residual image as shown clearly in Figure 6 top row (left and right panel for *nterms* = 1 and 2 respectively). Also, CLEANing the whole image to a deeper flux density threshold removes part of the diffuse structure. A shallow threshold, on the other hand, retains the diffuse emission but also significant residual point source contribution (see Figure 6 middle row). Finally, deep

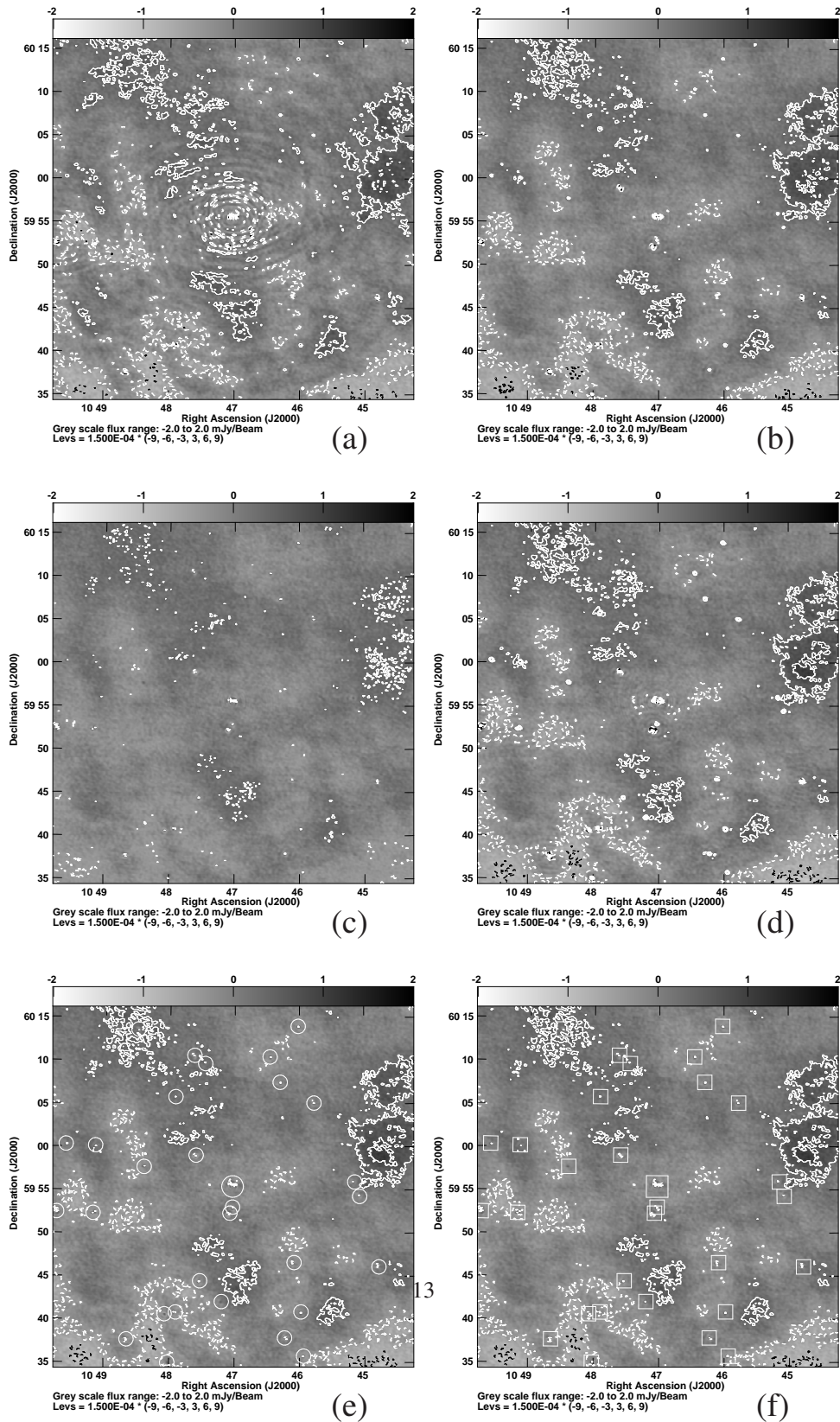


Figure 6: Residual images of the $42' \times 42'$ representative region for various CLEANING strategies listed in Table 1. The residual images Image(a), Image(b), Image(c), ..., and Image(f) correspond to Run(a), Run(b), Run(c), ..., and Run(f) respectively. The contour levels are $(-9, -6, -3, 3, 6, 9) \times 0.15$ mJy/Beam and the grey scale is in mJy/Beam.

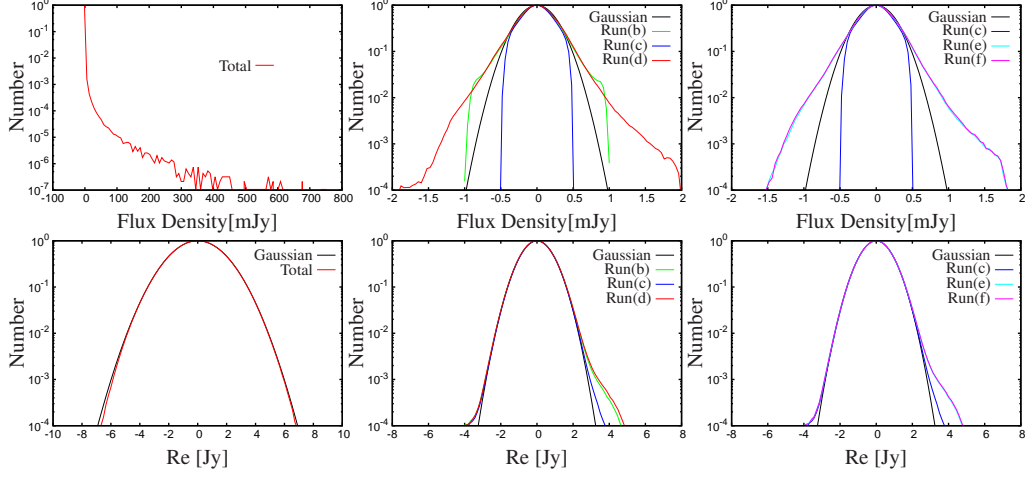


Figure 7: The distribution of image plane pixel values (upper row) and the real part of visibilities (lower row) before point source subtraction (left panels) and after point source subtraction (middle and right panels) for the runs mentioned in Table 1. The best fit Gaussian function for the distributions are also shown in each panel.

CLEANing ($\sim 1.5 \sigma_{im}$) in combination with carefully selected CLEANing regions results in the optimum residual images shown in the bottom row of Figure 6. In the next section, we assess impact of the different CLEAN strategies on the statistics such as distribution of visibilities and estimated angular power spectrum from these different residual data sets.

4. Results

We use different CLEANing options mentioned above for point source subtraction from a $4.2^\circ \times 4.2^\circ$ region of the sky from simulated visibility data. To compare the outcome of these strategies, we check the statistics of the residual visibilities as well as of the residual dirty images. In Figure 7 we show the normalized histograms from images (top row) and from the visibility data (bottom row). The top-left panel of Figure 7 shows the distribution of the pixel values from the initial CLEANed map (Figure 4) dominated by the diffuse emission (pixels with ≤ 5.0 mJy) and only a small number of pixels with high flux density (due to the bright point sources). The top middle and right panel show the histogram of the residual images from different CLEANing runs. A Gaussian with $\sigma = 0.228$ mJy is a fairly good fit to the distribution of the residuals up to a flux density limit of ± 0.5 mJy. However, as evident from the top central panel, “blind” CLEANing with lower threshold (see Table 1) makes residual images more non-Gaussian. On the other hand, for deep CLEANing using different CLEANing box options, there is no difference in the distribution of the residual images.

The corresponding visibility distribution functions are shown in the bottom row of Figure 7. We use the real part the complex visibilities for these plots, but the imaginary parts also have a similar distribution. We find that both the initial and residual visibilities have a Gaussian distribution, but with different standard deviation ($\sigma = 1.61$ Jy before point source subtraction and 0.76 Jy up to $|\text{Re}(V)| < 3$ Jy for the residual visibility). The counts significantly deviate from Gaussian distribution at large visibility values most likely due to incomplete CLEANing.

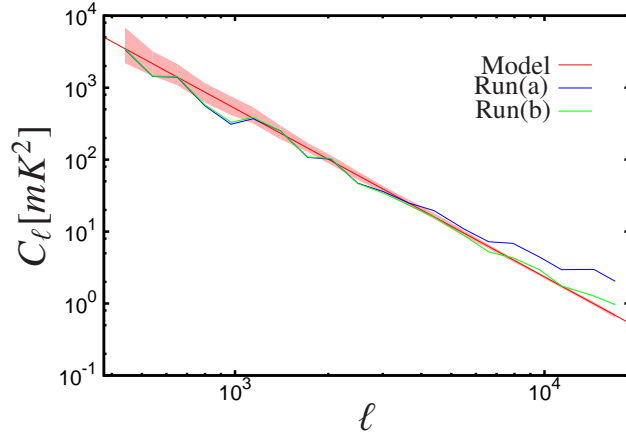


Figure 8: The estimated power spectra from residual visibility data for Run(a) and Run(b) corresponding to threshold flux density of 1 mJy with $n_{terms} = 1$ and 2 respectively. The solid line shows the input model (eq. 3) with $1\text{-}\sigma$ error estimated from 100 realizations of the diffuse emission map.

Next we use the residual visibilities from different runs to estimate the angular power spectrum C_ℓ using the TGE. Here, we have used logarithmic intervals of ℓ after averaging all the frequency channels. We have also used Gaussian window function to taper the sky response. The tapering is introduced through a parameter f , where f is preferably ≤ 1 so that modified window function cuts off the sky response well before the first null of the primary beam (see for details, Figure 1 of Choudhuri et al. 2016a). The reduced field of view results in a larger cosmic variance for the angular modes which are within the tapered field of view. So, the tapering parameter f will possibly be determined by optimizing between the reduced field of view and the cosmic variance. In this work we use $f = 0.8$. Figure 8 shows the estimated C_ℓ from the residual visibilities for Run(a) and Run(b), that is for fixed CLEANing threshold of 1.0 mJy but $n_{terms} = 1$ and 2 respectively. CLEANing with $n_{terms} = 2$ reduces the residual sidelobes around bright sources after point source subtraction (see Figure 6a,b). Hence, as shown in Figure 8, the estimated C_ℓ recover the input power spectrum better even at large ℓ ($\geq 6 \times 10^3$) clearly demonstrating the need of correct spectral modelling of the point sources.

The left panel of Figure 9 shows the angular power spectra C_ℓ estimated using the residual visibility data obtained from Run(b), (c) and (d) for $n_{terms} = 2$ but different CLEANing threshold. Run(b) with $\sim 3\sigma_{im}$ CLEANing threshold recovers C_ℓ for the entire range of ℓ , but Run(d) with shallow CLEANing retains some extra residual power at large ℓ ($\geq 7 \times 10^3$). The estimated C_ℓ from Run(c), on the other hand, falls off by a factor ~ 5 compared to the input model due to blind deep CLEANing that removes part of the underlying diffuse signal. The effect of using different CLEANing box options in recovering C_ℓ is shown in the right panel of Figure 9. Here we keep the other two parameters fixed at $n_{terms} = 2$ and threshold of 0.5 mJy. It is clear from this figure that there is no significant change in the estimated power spectra for the two different CLEANing box strategies used in Run(e) and (f). In both the cases, the estimated C_ℓ agree well with the input power spectrum over the full range of ℓ probed here.

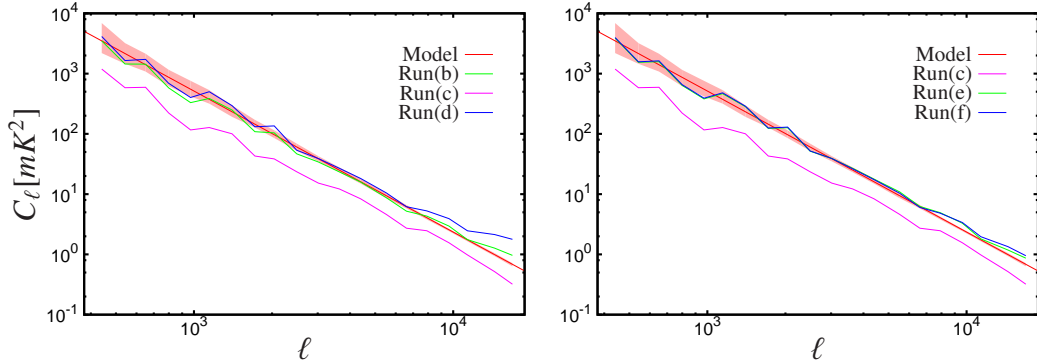


Figure 9: The left panel show the estimated power spectra using residual data from Run(b), (c) and (d) with different CLEANing threshold but fixed value of $n_{\text{terms}} = 2$. The right panel show the same but using residual data from Run(c), (e) and (f) with different CLEAN box options but fixed CLEANing threshold (see Table 1 for details).

5. Summary and conclusions

Precise subtraction of point sources from wide-field interferometric data is one of the primary challenges in studying the diffuse foreground emission as well as the weak redshifted HI 21-cm signal. In this paper, we demonstrate the method of studying and characterizing the Galactic synchrotron emission using simulated 150 MHz GMRT observation in presence of point sources. The angular power spectrum C_ℓ of the diffuse emission is estimated from the residual visibility data using TGE after subtracting the point sources from only the inner part of the field of view. The estimated C_ℓ due to faint point sources is much lower than the diffuse synchrotron emission. We assess the impact of imperfect point source removal for different CLEANing strategies in recovering the input C_ℓ of the diffuse emission for the angular scale range probed by the GMRT.

The simulations are carried out for GMRT 150 MHz observation for a sky model consisting of point sources and diffuse synchrotron emission. The sky model is multiplied with the model PB $\mathcal{A}(\vec{\theta}, \nu)$, before computing the visibilities for the frequency and the uv coverage of the simulated GMRT observation. We use various CLEANing strategies with different CLEANing boxes, threshold flux and spectral correction options to make images and to subtract point source model from the simulated visibilities. The residual data were then used for estimating C_ℓ of the diffuse component. We check the effect of point source subtraction by comparing image histograms, visibility distribution function as well as C_ℓ from the residual data.

We find that all the different CLEANing strategies introduce some degree of non-Gaussianity in the residual data both in image and in visibility domain. The less precise point source subtraction generates more non-Gaussianity in the distribution of image-pixels beyond the CLEANing threshold. Equivalently, the visibility distributions also deviate significantly from a Gaussian. Comparing the recovered and the input power spectra, we find that both shallow CLEANing and incorrect spectral modelling of the point sources result in excess power at the large angular multipoles. On the other hand, very deep “blind” CLEANing removes part of the diffuse structure and reduces the amplitude of the power spectrum at all angular scale. Carefully choosing CLEAN boxes for deep CLEANing (with threshold $\sim 1.5\sigma_{im}$) and correct spectral modelling of the point sources demonstrate that TGE can recover the input power spectrum of the diffuse emission properly. Note that this analysis also demonstrate that the effect of the point sources

from the outer region of the field is insignificant due to the tapering. Hence, while using TGE for power spectrum estimation, many of the complications discussed earlier related to the low frequency wide field imaging become irrelevant.

Finally, the accurate removal of all the point sources from the wide-field image is complicated and difficult task in presence of instrumental systematics, calibration errors, RFI and ionospheric effects etc. Using simulated data, we have established here the effectiveness of TGE in estimating the angular power spectrum C_ℓ of diffuse emission at the angular scales probed by the GMRT. This gives us the confidence to apply it on real data in order to study the Galactic synchrotron power spectrum (Choudhuri et al., 2017). With the broad goal of applying it in future for EoR and post-EoR HI studies, we plan to next incorporate some of the above mentioned “real world” issues in this simulation, and also extend this study for the SKA.

6. Acknowledgements

SC would like to acknowledge the University Grant Commission (UGC), India for providing financial support through Senior Research Fellowship. SSA would like to acknowledge CTS, IIT Kharagpur for the use of its facilities. SSA would also like to thank the authorities of the IUCAA, Pune, India for providing the Visiting Associateship programme. AG would like acknowledge Postdoctoral Fellowship from the South African Square Kilometre Array Project for financial support. **PD will like to acknowledge the DST-INSPIRE faculty fellowship by Department of Science and Technology, India for providing financial support.**

References

- Ali S. S., Bharadwaj S., & Chengalur J. N., 2008, MNRAS, 385, 2166A
 Ali, Z. S., Parsons, A. R., Zheng, H., et al. 2015, ApJ, 809, 61
 Bennett C.L., Hill R.S., Hinshaw, G. et al., 2003, ApJS, 148, 97
 Bernardi, G., de Bruyn, A. G., Brentjens, M. A., et al. 2009, A & A, 500, 965
 Bhatnagar, S., Rau, U., & Golap, K. 2013, ApJ, 770, 91
 Bowman, J. D., Morales, M. F., & Hewitt, J. N. 2009, ApJ, 695, 183
 Chapman, E., Abdalla, F. B., Harker, G., et al. 2012, MNRAS, 423, 2518
 Chapman, E., Zaroubi, S., Abdalla, F. B., et al. 2016, MNRAS, 458, 2928
 Choudhuri, S., Bharadwaj, S., Ghosh, A., & Ali, S. S., 2014, MNRAS, 445, 4351
 Choudhuri, S., Bharadwaj, S., Roy, N., Ghosh, A., & Ali, S. S. 2016a, MNRAS, 459, 151
 Choudhuri, S., Bharadwaj, S., Chatterjee, S., et al. 2016b, MNRAS, 463, 4093
 Choudhuri, S., Bharadwaj, S., Saiyad Ali, S., et al. 2017, arXiv:1704.08642
 Conway, J. E., Cornwell, T. J., & Wilkinson, P. N. 1990, MNRAS, 246, 490
 Cornwell, T. J., Golap, K., & Bhatnagar, S., 2008, IEEE Journal of Selected Topics in Signal Processing, 2, 647
 Datta, A., Bhatnagar, S., & Carilli, C. L. 2009, ApJ, 703, 1851
 Datta, A., Carilli, C. L., Bhatnagar, S., & Bowman, J. D. 2010, Bulletin of the American Astronomical Society, 42, 325.02
 Datta, A., Bowman, J. D., & Carilli, C. L. 2010a, ApJ, 724, 526
 Dillon, J. S., Liu, A., & Tegmark, M. 2013, PRD, 87, 043005
 Di Matteo, T., Perna, R., Abel, T. & Rees, M.J., 2002, ApJ, 564, 576
 Frigo, M., & Johnson, S. G. 2005, Proceedings of the IEEE, 93, 216
 Ghosh, A., Prasad, J., Bharadwaj, S., Ali, S. S., & Chengalur, J. N. 2012, MNRAS, 426, 3295
 Giardino, G., Banday, A. J., Górski, K. M., et al. 2002, A & A, 387, 82
 Harker, G., Zaroubi, S., Bernardi, G., et al. 2010, MNRAS, 405, 2492
 Hazelton, B. J., Morales, M. F., & Sullivan, I. S. 2013, ApJ, 770, 156
 Iacobelli, M., Haverkorn, M., Orrú, E., et al. 2013, A & A, 558, A72
 Intema, H. T., van der Tol, S., Cotton, W. D., et al. 2009, A & A, 501, 1185
 Jackson, C. 2005, PASA, 22, 36

Jelić, V., Zaroubi, S., Labropoulos, P., et al. 2008, MNRAS, 389, 1319
 Jelić, V., Zaroubi, S., Labropoulos, P., et al. 2010, MNRAS, 409, 1647
 La Porta, L., Burigana, C., Reich, W., & Reich, P. 2008, A & A, 479, 641
 Lazarian, A., & Pogosyan, D. 2012, ApJ, 747, 5
 Liu, A., Tegmark, M., & Zaldarriaga, M. 2009a, MNRAS, 394, 1575
 Liu, A., Tegmark, M., Bowman, J., Hewitt, J., & Zaldarriaga, M. 2009b, MNRAS, 398, 401
 Liu, A., & Tegmark, M. 2012, MNRAS, 419, 3491
 Liu, A., Parsons, A. R., & Trott, C. M. 2014a, PRD, 90, 023018
 Liu, A., Parsons, A. R., & Trott, C. M. 2014b, PRD, 90, 023019
 Mao, X.-C. 2012, ApJ, 744, 29
 Moore, D. F., Aguirre, J. E., Parsons, A. R., Jacobs, D. C., & Pober, J. C. 2013, ApJ, 769, 154
 Morales, M. F., Bowman, J. D., & Hewitt, J. N. 2006, ApJ, 648, 767
 Morales, M. F., Hazelton, B., Sullivan, I., & Beardsley, A. 2012, ApJ, 752, 137
 Offringa, A. R., Trott, C. M., Hurley-Walker, N., et al. 2016, MNRAS, 458, 1057
 Paciga G. et al., 2011, MNRAS, 413, 1174
 Paciga, G., Albert, J. G., Bandura, K., et al. 2013, MNRAS, 433, 639
 Parsons, A. R., Pober, J. C., Aguirre, J. E., et al. 2012, ApJ, 756, 165
 Pindor, B., Wyithe, J. S. B., Mitchell, D. A., et al. 2011, PASA, 28, 46
 Platania, P., Bensadoun, M., Bersanelli, M., de Amici, G., Kogut, A., Levin, S., Maino, D., & Smoot, G. F. 1998, ApJ, 505, 473
 Pober J. C. et al., 2013, ApJL, 768L, 36
 Pober, J. C., Hazelton, B. J., Beardsley, A. P., et al. 2016, ApJ, 819, 8
 Randall, K. E., Hopkins, A. M., Norris, R. P., et al. 2012, MNRAS, 421, 1644
 Rau, U., & Cornwell, T. J., 2011, A & A, 532, A71
 Santos, M. G., Cooray, A., & Knox, L. 2005, ApJ, 625, 575
 Sault, R. J., & Wieringa, M. H. 1994, Astronomy and Astrophysics, Supplement, 108,
 Shaver, P. A., Windhorst, R. A., Madau, P., & de Bruyn, A. G. 1999, A & A, 345, 380
 Schwab, F. R., 1984, AJ, 89, 1076
 Tegmark M. & Efstathiou G., 1996, MNRAS, 281, 1297
 Tegmark, M., Eisenstein, D. J., Hu, W., & de Oliveira-Costa, A. 2000, ApJ, 530, 133
 Thompson, A.R., Moran, J.M., & Swenson, G.W. 1986, Interferometry and Synthesis in Radio Astronomy, John Wiley & Sons, pp. 160
 Thyagarajan, N., Udaya Shankar, N., Subrahmanyan, R., et al. 2013, ApJ, 776, 6
 Trott, C. M., Wayth, R. B., & Tingay, S. J. 2012, ApJ, 757, 101
 Trott, C. M., Pindor, B., Procopio, P., et al. 2016, ApJ, 818, 139
 Vedantham, H., Udaya Shankar, N., & Subrahmanyan, R. 2012, ApJ, 745, 176
 Waelkens, A. H., Schekochihin, A. A., & Enßlin, T. A. 2009, MNRAS, 398, 1970
 Yatawatta, S. 2012, Experimental Astronomy, 34, 89